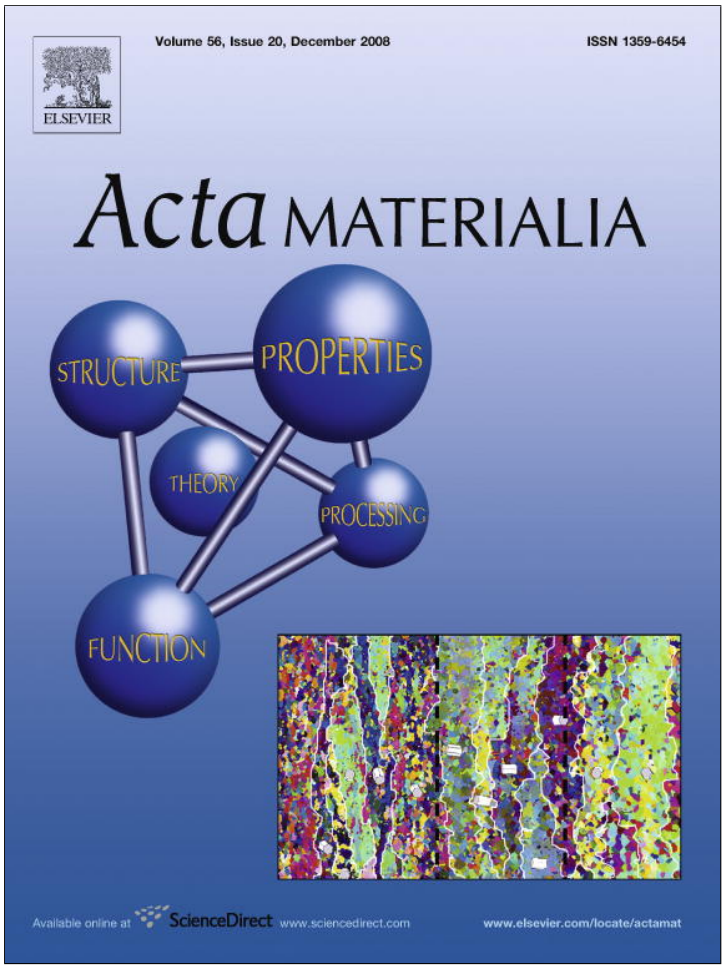

Available online at www.sciencedirect.com
ScienceDirect
Acta Materialia 56 (2008) 6123–6131
Acta MATERIALIA
www.elsevier.com/locate/actamat

Thermal evolution and grain boundary phase transformations in severely deformed nanograined Al–Zn alloys

B. Straumal [a,b,*], R. Valiev [c], O. Kogtenkova [a], P. Zieba [d], T. Czeppe [d], E. Bielanska [d], M. Faryna [d]

[a] Institute of Solid State Physics, Russian Academy of Sciences, 142432 Chernogolovka, Moscow District, Russia
[b] Max-Planck-Institut für Metallforschung, Heisenbergstrasse 3, 70569 Stuttgart, Germany
[c] Ufa State Aviation Technical University, 450000 Ufa, Russia
[d] Institute of Metallurgy and Materials Science, Polish Academy of Sciences, Reymonta Street 25, 30-059 Cracow, Poland

Received 5 October 2007; received in revised form 14 August 2008; accepted 15 August 2008
Available online 15 September 2008

Abstract

The structure, phase composition and thermal evolution of binary Al–Zn alloys were studied before and after high-pressure torsion (HPT) in Bridgman anvils. On heating of HPT-deformed samples from room temperature to 300 °C, Zn grains dissolved, and a relatively fine-grained (Al) equilibrium solid solution formed. Differential scanning calorimetry curves reveal two-stage melting in the Al–Zn alloys studied, i.e., the melting of the (Al) solid solution starts 10–25 °C below the bulk solidus line. The effect is more pronounced in fine-grained samples. It is explained by the presence of layers of liquid-like phase in the (Al) grain boundaries (GB) between bulk and GB solidus lines. The new metastable GB solidus line appears in the (Al) single-phase region of the Al–Zn phase diagram, it can be compared with the metastable solvus lines for the formation of GP zones and α phases in the (Al)+Zn two-phase area.

Keywords: Grain boundaries; Severe plastic deformation; Al–Zn alloys; Wetting phase transition

1. Introduction

The manufacture of materials with a very small grain size in the nanometre range is an important way of improving the mechanical properties of metallic materials [1,2]. In particular, such nanograined alloys possess higher strength in comparison with coarse-grained (CG) ones. At the same time, they conserve reliable plasticity. In special cases, in the narrow interval below the solidus line, fine-grained Al–Mg–Zn alloys possess n extremely high plasticity up to 2500% [3,4]. The reason for the superplasticity of these Al-based alloys as well as for the high diffusivity in Cu–Bi and Fe–Si–Zn alloys may be the formation of liquid-like layers of grain boundary (GB) phases [5–8]. The influence of such GB layers on the overall properties of polycrystals will be especially pronounced in micro- and nanograined materials.

Very promising techniques for obtaining bulk nanograined materials include different variants of severe plastic deformation (SPD). Such SPD techniques as equal channel angular pressing (ECAP) and high-pressure torsion (HPT) do not involve changes in the material geometry, in contrast to the conventional processes of high deformation such as rolling or wire drawing. The severe plastic deformation of binary Al–Zn, Al–Mg, and ternary Al–Zn–Mg alloys was studied in previous work [9–12]. It was demonstrated that, during HPT, the Zn-containing (Al) supersaturated solid solution decomposes completely and closely approaches the equilibrium state corresponding to room temperature. The authors concluded that the severe plastic deformation of supersaturated solid solutions could be considered a balance between deformation-induced

* Corresponding author. Address: Institute of Solid State Physics, Russian Academy of Sciences, 142432 Chernogolovka, Moscow District, Russia. Tel.: +79166768673; fax: +74992382326.
E-mail address: straumal@issp.ac.ru (B. Straumal).

1359-6454/$34.00 © 2008 Acta Materialia Inc. Published by Elsevier Ltd. All rights reserved.
doi:10.1016/j.actamat.2008.08.021

disordering and deformation-accelerated diffusion, bringing the alloys closer to equilibrium.

In the as-cast state, the hardness of the supersaturated solid solutions increases with increasing Zn and Mg content, owing to the solid solution hardening. However, after HPT, the work hardening and Hall–Petch hardening due to the decreasing grain size compete with softening due to the decomposition of a supersaturated solid solution. In the net effect, the severe plastic deformation resulted in the softening of binary Al–Zn and Al–Mg alloys [11,12]. Softening is more pronounced in Al–Zn alloys, where the HPT leads to the almost full decomposition of the supersaturated solid solution. First, differential scanning calorimetry (DSC) investigations of the ECAP-deformed Al-7034 and Al-2024 alloys demonstrated that their thermal evolution is quite different from that of conventional CG materials [13,14]. Therefore, the processes of structural changes during SPD are very complicated and have not been yet fully understood. The goal of this work is the investigation of thermal evolution in severely deformed fine-grained Al–Zn alloys and the possible input of grain boundary phase transformations. Al–Zn alloys were chosen because of their quick diffusion relaxation during the thermal treatments.

2. Experimental

Aluminium-based alloys of the following compositions were investigated: Al–10 wt.% Zn, Al–16 wt.% Zn, Al–17.5 wt.% Zn, and Al–24 wt.% Zn. The alloys were prepared from high-purity components (5N5 Al and 5N Zn) by vacuum induction melting. As-cast disks of these alloys obtained after grinding, sawing and chemical etching were subjected to HPT at room temperature under a pressure of 5 GPa in a Bridgman anvil-type unit (five torsions, duration process ~300 s) [15]. All samples for structural and calorimetric investigations were cut from the deformed disks at a distance of 5 mm from the sample centre. For this distance, the shear strain is ~6. Transmission electron microscopy (TEM) investigations were carried out in a Philips CM 20 microscope equipped with an energy-dispersive spectrometer at an accelerating voltage of 400 kV. Scanning electron microscopy (SEM) investigations were carried out on a Philips XL30 scanning microscope equipped with a LINK ISIS energy-dispersive spectrometer produced by Oxford Instruments. Measurements by differential scanning calorimetry (DSC) were performed using TA Instruments 910 and 1600 calorimeters.

The 2-mm-thick slices were also cut from the ∅10 mm cylindrical Al–Zn ingots and sealed into evacuated silica ampoules with a residual pressure of $\sim 4 \times 10^{-4}$ Pa at room temperature. Samples were annealed at 200 °C (4000 h), 230 °C (1200 h), 250 °C (1000 h), 270 °C (800 h) and 280 °C (800 h), and then quenched in water. The accuracy of the annealing temperature was ±2 °C. After quenching, samples for TEM investigations were cut from the specimens. The residual material was embedded in resin and then mechanically ground and polished, using 1-μm diamond paste in the last polishing step, for the metallographic study. After etching, samples were investigated by means of the light microscopy, SEM and electron back-scattering diffraction (EBSD). Light microscopy was performed using a Neophot-32 light microscope equipped with a 10 Mpix Canon Digital Rebel XT camera. EBSD maps were obtained using a FEI E-SEM XL30 scanning microscope equipped with NORDIF EBSD hardware at acceleration voltage 20 kV, tilt angle 70° and working distance 16 mm detector, using CHANNEL 5 EBSD software for the orientation imaging microscopy.

3. Results

Fig. 1 shows the bright-field TEM micrograph for the Al–24 wt.% Zn alloy after HPT. Specimens of all studied Al–Zn alloys after HPT have two phases, and two types of grains are observed in the structure (Fig. 1). These are grains of (Al) solid solution 1 μm in size (instead of 500 μm before HPT), and grains of Zn ~200 nm in size (instead of 3–5 μm before HPT). (Al) grains appear grey and Zn grains appear black in Fig. 1. This was revealed by the local concentration measurements. (Al) grains are almost Zn free. Zn content in the (Al) grains after HPT is <1 wt.% (measured in TEM by scanning energy-dispersive spectrometry). This value corresponds to Zn solubility in Al at room temperature. Al content in Zn grains is negligible; this fact also corresponds to the equilibrium Al–Zn phase diagram [14].

In Fig. 2, the DSC curves (dependences of heat flow on the temperature) are shown for the Al–17.5 wt.% Zn samples for heating from 20 to 300 °C. The temperature of 300 °C is higher than the temperature of monotectoid transformation in the Al–Zn system. At 300 °C, all alloys studied are in the one-phase (Al) solid solution area of the Al–Zn phase diagram [14]. Samples after HPT were heated in the same temperature interval with two different

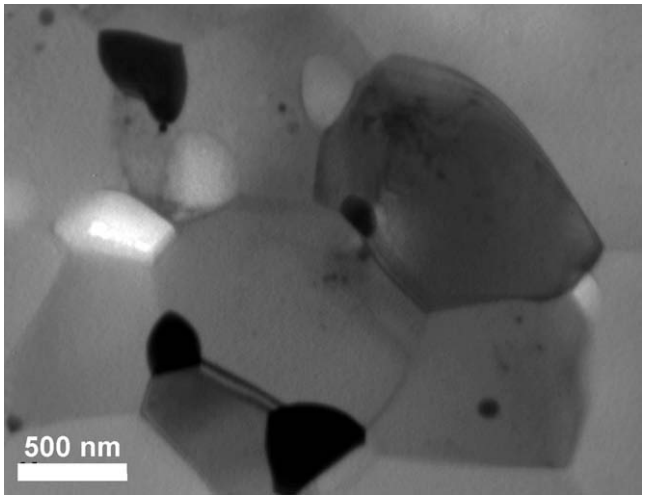

Fig. 1. Bright-field TEM micrograph for the Al–24 wt.% Zn alloy after HPT.

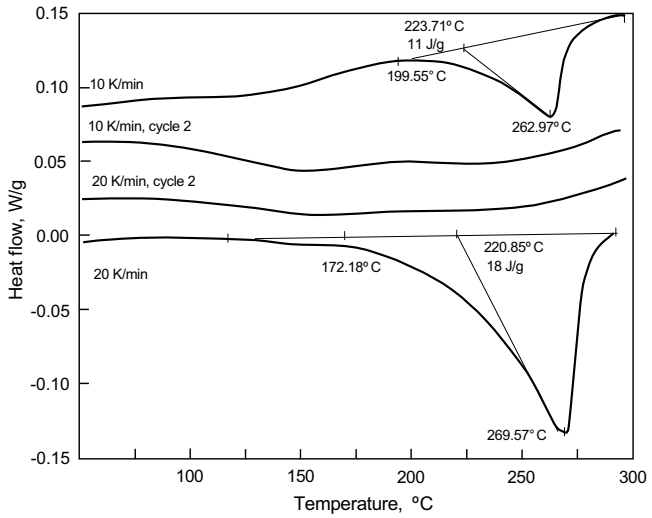

Fig. 2. Temperature dependence of heat flow (DSC curve) for the Al–17.5 wt.% Zn samples. After HPT, samples were heated at a rate of 10 K min^{-1} (upper curve) and 20 K min^{-1} (lower curve). After these measurements, the same samples were cooled down and heated again with the same heating rates as in the first cycle (two curves between upper and lower curves, the second cycle).

rates, namely 10 and 20 K min^{-1}. At a lower heating rate of 10 K min^{-1} (upper curve), only one deep endothermic minimum at 263 °C is visible. By 20 K min^{-1} (lower curve), this minimum is shifted towards 270 °C. After heating from 20 to 300 °C, the samples were cooled down and heated again with the same heating rates as in the first cycle (two curves in the middle, second cycle). Both curves after the second cycle are slightly concave, but do not possess any pronounced minimum.

Fig. 3 shows the bright-field TEM micrograph for the Al–24 wt.% Zn alloy after HPT and one 20–300 °C heating cycle in a DSC calorimeter. The (Al) grain size increased from 1 μm before the heating cycle to ~10–30 μm after heating to 300 °C. Zn grains disappeared. The concentration

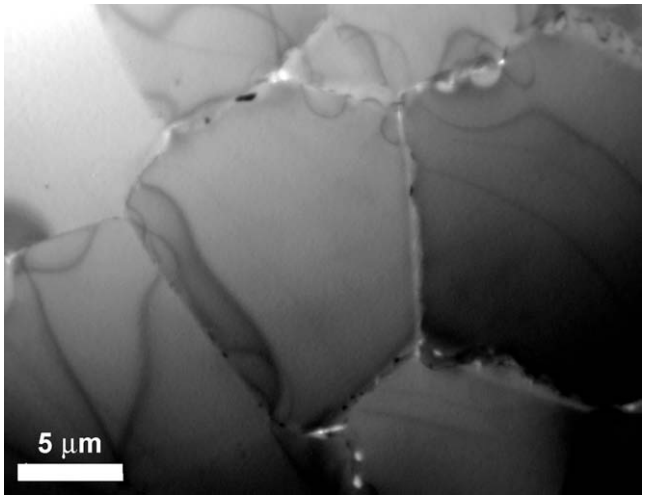

Fig. 3. Bright-field TEM micrograph for the Al–24 wt% Zn alloy after HPT and one DCS cycle (heating from 20 to 300 °C).

measurements show that Zn particles almost fully dissolved in (Al) grains. However, the Zn is not uniformly distributed in (Al). Zn concentration is higher close to the GB in (Al). TEM reveals that, after the second 20–300 °C heating cycle, the (Al) grain size increased further to ~30–50 μm. The Zn content in (Al) became almost uniform.

The microstructure shown in Fig. 3 was the starting point for the high-temperature DSC experiments. Fig. 4 shows DSC curves for the Al–Zn samples with 10, 16 and 24 wt.% Zn for heating from 20 to 670 °C at a rate of 20 K min^{-1}. Only the high-temperature part between 570 and 670 °C is shown. For the Al–Zn alloys with 16 and 24 wt.% Zn, curves for both as-cast CG and fine-grained HPT-samples are shown. According to the standard approach to the quantification of DSC curves of the alloys melting between solidus and liquidus temperatures [17] (these procedures are also included in the quantification software of modern DSC equipment), the position of a deep minimum corresponds to the end of melting, i.e., to the liquidus temperature. The measured minima positions (Fig. 4) for all samples correspond well to the literature data for the liquidus in the Al–Zn bulk phase diagram (Fig. 5 [16]). In Fig. 5, the high-temperature part of the Al–Zn bulk phase diagram close to the Al melting point is shown [16]. Thick lines denote the liquidus and solidus for bulk (Al) alloys. Open circles in Figs. 4 and 5 denote the positions of minima in DSC curves. The minimum temperatures for the HPT-samples coincide with those for the CG alloys.

According to the same standard approach [17], the solidus temperature was defined using the linear tangential

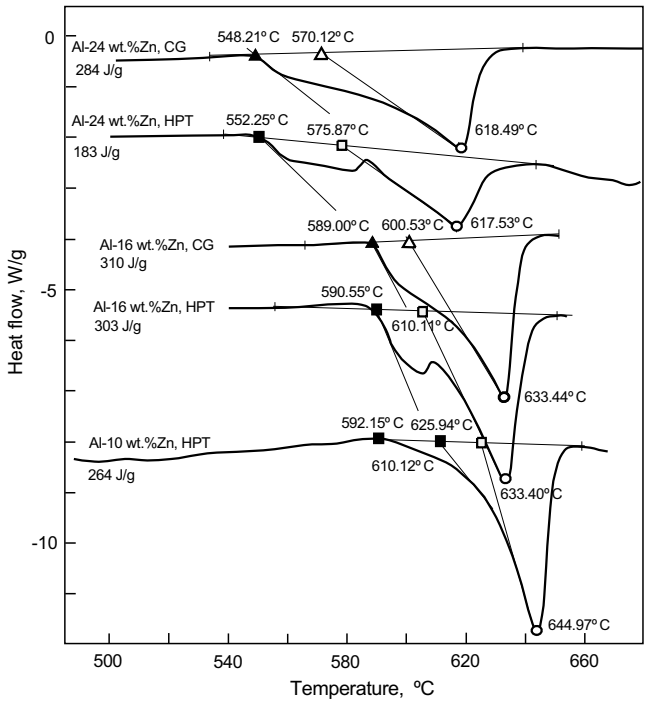

Fig. 4. Temperature dependence of heat flow (DSC curves) for the Al–Zn samples: ○, liquidus temperature; △, bulk solidus for CG alloys; □, bulk solidus for fine-grained (HPT) alloys; ▲, GB solidus for CG alloys; ■, GB solidus for fine-grained (HPT) alloys.

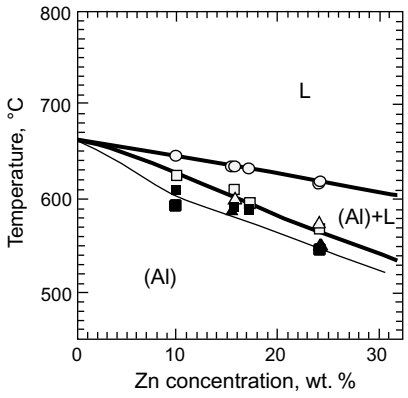

Fig. 5. Part of the Al–Zn phase diagram. Thick lines mark the bulk liquidus and solidus [16]. Thin lines mark GB solidus. Experimental points are taken from Fig. 4. ○, liquidus temperature; △, bulk solidus for CG alloys; □, bulk solidus for fine-grained (HPT) alloys;, ▲, GB solidus for CG alloys; ■, GB solidus for fine-grained (HPT) alloys.

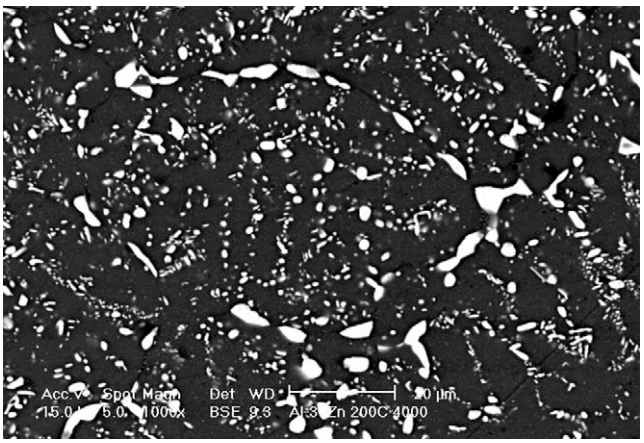

Fig. 6. SEM micrograph for the Al–24 wt.% Zn alloy annealed at 200 °C for 4000 h. Zn precipitates appear white. The surrounding (Al) solid solution appears dark. Two types of Zn particles are visible: (1) lens-like particles 2–10 μm in size arranged in chains; and (2) small round particles 1 μm in size and lower arranged in arrays (walls).

on the low-temperature side of the melting minimum and its intersection point with the base line. These intersection points are marked in Figs. 4 and 5 by open squares (HPT samples) and open triangles (CG samples). These intersection points for HPT and CG alloys are very close to each other (though less close than the minimum points). Both full and open triangles coincide well with the solidus line in the Al–Zn bulk phase diagram (Fig. 5). In the standard case [17], the left-hand side of the DSC minima for the melting follows the linear tangent almost until the intersection point with the base line. In the present case, the DSC line deviates from this tangential. Even more, the shallow second minimum is visible in DSC curves for the fine-grained HPT Al–16 wt.% Zn and Al–24 wt.% Zn alloys. These "shoulders" positioned to the left of the main DSC minima reveal the second, weak melting process in the samples. It is possible to draw the second tangential at lower temperatures in comparison with the "main" melting tangential. The intersection points of these second tangentials are marked in Figs. 4 and 5 by full squares (HPT samples) and full triangles (CG samples). They lie ~10–25 °C below the bulk solidus line (Fig. 5).

Long annealing of as-cast alloys between 200 and 280 °C allowed the morphology of Zn particles to be determined. In Fig. 6, the SEM micrograph is shown for the Al–24 wt.% Zn alloy annealed at 200 °C for 4000 h. Zn particles appear white and the (Al) matrix appears black in the micrograph. Two types of Zn particles are visible: (1) lens-like particles 2–10 μm in size arranged in chains; and (2) small round particles <1 μm in size arranged in arrays (walls) with thickness ~2–3 μm. The EBSD map for the same sample (Fig. 7) visualizes the grain orientations by different brightness, and marks the high-angle GB (with misorientation angle above 10°). The Zn precipitations appear white in Fig. 7. Big Zn particles are arranged along the high-angle GB. Chains of small particles are positioned inside the grains. EBSD revealed that arrays of small, round precipitates coincide with small-angle GBs (with misorientation angle between 2° and 5°). The mean contact angle between lens-like Zn particles and GB (Al)/(Al) can be estimated. It is ~60°. When the temperature is increased, the mean contact angle decreases to ~30° at 270 °C (temperature slightly below the monotectoid temperature of 277 °C) but remains above zero.

4. Discussion

The TEM investigations reveal that, as observed earlier [3–6], in the as-cast Al–Zn alloys about half the Zn is in the supersaturated (Al) solid solution. As a result of HPT, the

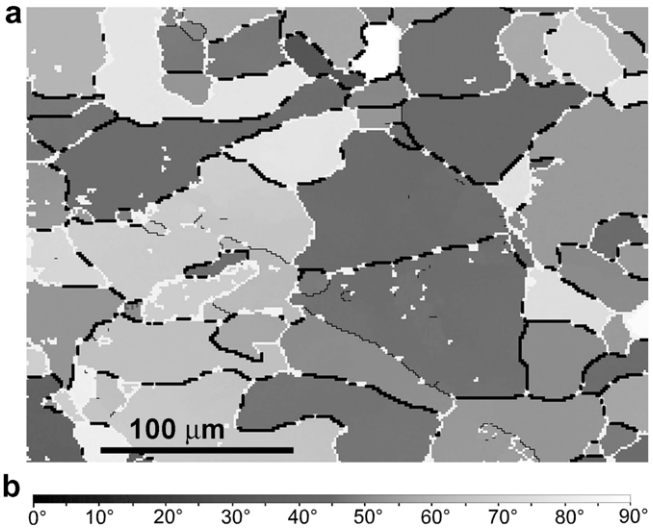

Fig. 7. EBSD map for the Al–24 wt.% Zn alloy annealed at 200 °C for 4000 h. Zn precipitates appear white. Greyscale visualizes the grain orientations (angle between the sample plane and <1 1 1> axis or the respective grain). High-angle GBs (misorientation angle >10°) are represented by thick lines and big brightness contrast. Arrays of small, round Zn precipitates coincide with small-angle GB (shown by thin lines, with misorientation angle between 2° and 5°).

Zn-containing (Al) supersaturated solid solution decomposes completely and closely approaches the equilibrium state corresponding to room temperature (<1 wt.% of Zn dissolved in Al [16]). The grain size decreases drastically after HPT. The size of (Al) grains decreases from 500 μm before HPT to ~1 μm after HPT. The size of Zn grains decreases from 3–5 μm before HPT to 200 nm after HPT. This was the starting microstructure before the DSC experiments (Fig. 1).

The decomposition is less pronounced for Al–Mg and Al–Mg–Zn alloys [9,10]. Thus, the severe plastic deformation of supersaturated solid solutions could be considered a balance between deformation-induced disordering and deformation-accelerated diffusion, bringing the alloys closer to equilibrium. In other words, HPT can be regarded as a hot deformation at room temperature. SPD leads first to the formation of lattice defects, including the non-equilibrium GB. These defects initiate the enhanced diffusion and lead in turn to the equilibration of phases during SPD. Zn has higher bulk and GB diffusivity in Al compared with Mg. As a result, the decomposition of Al–Zn supersaturated solid solution proceeds earlier than that of Al–Mg or Al–Zn–Mg supersaturated solid solutions [9,10]. The steady state is already reached in Al–Zn during HPT after one anvil torsion.

In DSC, the rate of heat absorption or emission dQ/dt by the sample is measured as a function of temperature. In the absence of any significant thermal events, the position of the baseline in such a plot is proportional to the specific heat of the sample [18]. The presence of an endothermic peak superimposed on the baseline indicates the occurrence of a heat-absorbing event, such as melting or species dissolution. However, an exothermic peak can occur as a result of some sort of heat-releasing event, such as solidification or precipitation. The area under a peak is proportional to ΔQ, the heat absorbed or released by the sample over the temperature range of the peak. During the heating of HPT-deformed fine-grained alloys, only one endothermic process was observed around 270 °C (Fig. 2, upper and lower curves). The minimum shifted slightly from 263 °C to 270 °C with an increase in heating rate from 10 to 20 K min^{-1}. These temperatures are slightly below the monotectoid temperature of 277 °C in the Al–Zn system [16]. Therefore, the minimum in a DSC curve can be attributed to the complete dissolution of Zn grains and the formation of (Al) solid solution. After the first heating cycle, the (Al) grains increase from 1 μm before heating cycle to ~10–30 μm after heating to 300 °C. The Zn grains disappear (Fig. 3). They almost fully dissolve in (Al) grains. Repeated heating of samples after the first heating cycle no longer reveals the deep minimum (Fig. 3, the curves in the middle). This is because the (Al) solid solution is almost completely formed during the first heating cycle. Both the second cycle curves in Fig. 3 are slightly concave. This can be explained by further equilibration of the (Al) solid solution, as Zn is not uniformly distributed in (Al). Usually, when the supersaturated Zn-rich Al-based solid solution decomposes, the particles of an equilibrium β(Zn) phase do not appear immediately in the bulk: the pre-precipitates and metastable phases with increasing Zn content appear one after the other. The usual sequence is: Guinier–Preston (GP) I zones (spherical pre-precipitates coherent with Al-matrix) → GP II zones (semi-coherent ellipsoidal pre-precipitates) → rhombohedral distorted fcc α_R phase → distorted fcc α_m phase → β(Zn) equilibrium phase [19]. The solvus lines for the formation of these metastable phases lie in the (Al) + β(Zn) two-phase area of the Al–Zn phase diagram below the stable solvus line for the formation of the β(Zn) equilibrium phase [20]. Below these metastable solvus lines is the line for the spinodal decomposition [20]. The DSC curves for the aged Al–Zn alloys contain one to three overlapping endothermal peaks for the dissolution of GP zones and α phases [20–24]. These peaks lie at temperatures between 70 and 170 °C, i.e., well below the stable solvus line and the position of endothermal peak in the present work (Fig. 2). The total thermal effect at a heating rate of 20 K min^{-1} is between 8 and 12 J g^{-1} in the Al–15 wt.% Zn alloy [20], ~5.9 J g^{-1} in the Al–10 wt.% Zn alloy, and quite small at 0.8 J g^{-1} in the Al–5 wt.% Zn alloy [21]. The temperature of the dissolution peak also decreases in this sequence. Using the Al–13.5 wt.% Zn alloy, Hirano and Hori [23] determined the dissolution enthalpies of 7.3 and 5.9 J g^{-1} for the GP(I) and GP(II) zones formed at 70 and 160 °C, respectively. In the present case, HPT leads to full decomposition of the supersaturated solid solution and to the formation of the equilibrium β(Zn) phase. As a result, the dissolution of this phase proceeds at a higher temperature (close to 270 °C) and with a higher thermal effect of 18.15 J g^{-1} than that of the dissolution of metastable phases in the Al–Zn alloys (70–170 °C and 0.8–12 J g^{-1}).

It must be emphasized that no exothermal peaks were observed in the DSC curves for the aged or HPT-deformed Al–Zn alloys either in the present work (Fig. 2) or in the literature [20–24]. The situation is more complicated in the Al–Zn–Mg alloys containing other additives such as Cu, Zr or Sc [13,14,21,25–27]. The supersaturated solid solution transforms in such alloys (with or without formation of GP zones) to the metastable η phase and then to the stable $\eta(MgZn_2)$ phase. As a result, a complicated sequence of endothermal and exothermal peaks can be observed in the DSC curves. Nevertheless, the heat effect of the endothermal dissolution of the metastable phase is ~5–11 J g^{-1} [13,14,21,25] and is, therefore, always lower than the effect of full Zn dissolution in this work (18.15 J g^{-1}). However, the thermal effect of full dissolution of the stable $\eta(MgZn_2)$ phase is ~20 J g^{-1} and higher [14,25] and is comparable with the thermal effect of full dissolution of the equilibrium β(Zn) phase in the Al–Zn alloys after HPT (Fig. 2). The heating processes shown in Fig. 2 finish at 300 °C, i.e., in the one-phase solid solution area of the Al–Zn system [16]. Note that the equilibration processes (such as precipitation by the decomposition of supersaturated solid solution or coarsening of the lamellar

structure) proceed discontinuously in the Al–Zn system, namely by the migration of GB between supersaturated grains and fine-lamellar (Al) + Zn colonies, or between fine-lamellar and coarse-lamellar areas [28–30]. This process is controlled by GB diffusion.

Most probably, GB diffusion accompanied by the formation of non-equilibrium vacancy fluxes during the severe torsion is responsible for the quick decomposition of the Al–Zn supersaturated solid solution [9]. In Al–Zn alloys, the supersaturated solid solution with a concentration of ~12 wt.% completely decomposes after 300 s of HPT at room temperature. The supersaturation is the driving force for the bulk and GB diffusion of Zn from the solid solution to the sinks being the particles of (Zn). The diffusion paths for the individual Zn atoms would be ~800 nm. It corresponds to the bulk diffusion coefficients of 10^{-15} m^2 s^{-1}. The extrapolation of the tracer diffusion data for bulk diffusion of Zn in Al [31,32] to room temperature delivers the value D (300 K) = 10^{-23} m^2 s^{-1}. This is ~8 orders of magnitude less than the value estimated from the diffusion path of the actual solid solution decomposition during HPT. The mean distance between Zn particles in the nanostructured Al–30 wt.% Zn alloy is ~2 μm. This means that each particle collected the Zn atoms from the surrounding with radius (diffusion path) of ~2 μm. This area includes several (Al) grains and many (Al) GB. The transport of Zn from the (Al) matrix can be controlled by GB diffusion of Zn atoms along (Al) GB. Suppose that the moving GB during HPT swept each Zn atom in the bulk at least once, and then bulk diffusion towards a GB does not have to be considered. In this case, the path for GB diffusion would be roughly 1 μm, yielding an $sD\delta$ value of 1.5×10^{-24} m^3 s^{-1} for a GB thickness $\delta = 0.5$ nm and a segregation factor $s = 1$. The extrapolation of Zn GB diffusion data in Al polycrystals and bicrystals obtained by various methods [33–36] to room temperature yields the $sD\delta$ values between 10^{-29} and 10^{-24} m^3 s^{-1}. If GB diffusion is so effective, why does the supersaturated solid solution not decompose without any HPT? The reason is the low bulk diffusivity. The solute atoms are frozen in the bulk and cannot reach the GB. During HPT, GB move and cross every element of the volume many times, sweeping in such a way the "frozen" solute atoms. This mechanism is to a certain extent opposite to the well-known diffusion-induced grain boundary migration (DIGM). Therefore, the explanation for the quick decomposition of the supersaturated (Al) solid solution can be the formation of the non-equilibrium vacancies during deformation and their migration to the sinks. Early estimations of vacancy production during cold work were made based on data for residual resistivity measurements [37]. From the residual resistivity per Frenkel pair, deduced from irradiation experiments, it was concluded that atomic concentrations of 10^{-5}–10^{-4} are reached for strains $\varepsilon \approx 1$ [38,39]. Therefore, even a strain of $\varepsilon \approx 1$ produces a vacancy concentration comparable with the equilibrium value at melting point (~10^{-4} [37]).

DSC curves measured in Al-based alloys usually finish below the melting temperature [18–27]. The beginning of melting can be seen only in the DSC curves obtained on the ECAP-deformed Al-7034 and Al-2024 alloys [13,14]. The thermal effect of the melting in the present samples is between 183 and 310 J g^{-1} (Fig. 4). It is ~10–20 times higher than the relatively small heat of Zn dissolution in (Al)-matrix (Fig. 2) and ~40% lower than the heat of melting of pure Al (399.9 ± 1.3 J g^{-1} [40] and 401.3 ± 1.6 J g^{-1} [41]). The present data are close to the melting heat of Al–34 wt.% Mg–6 wt.% Zn alloy studied as the materials for latent heat storage [42]. In the freshly prepared Al–34 wt.% Mg–6 wt.% Zn alloy, the melting heat was 329 J g^{-1}. However, it decreased to 292 J g^{-1} after multiple melting–solidification cycles [42].

The main unusual result obtained in this work is that the melting of the Al–Zn alloys studied (especially that of fine-grained HPT ones) proceeds in two stages (Fig. 4). The small endothermic satellite peak is visible at temperatures just below the main endothermic melting peak. It becomes weaker with increasing grain size. The heat of this process can be estimated as ~15–25% of the whole thermal effect of melting. This phenomenon can be explained by the existence of the GB solidus line below the bulk solidus line in the Al–Zn system. In other words, the layer of GB liquid-like phase is present in Al–Zn alloys just below the solidus line. The structural indications of such GB liquid-like phase were observed in Al–Zn alloys by TEM [6]. The GB liquid-like phase drastically influences the GB diffusivity [5,8], GB segregation [7], GB mobility [43], GB energy and electrical resistivity [44,45]. According to the theory of pre-melting or pre-wetting phase transitions, the thin GB liquid-like layer appears by the intersection of the GB solidus line, and its thickness logarithmically increases by approaching from the GB solidus to the bulk solidus line [46,47]. At the bulk solidus line, the GB liquid-like phase transforms into a conventional liquid phase, and its thickness becomes macroscopic (i.e., a few microns). If the thickness of the GB liquid layer close to the bulk solidus is ~2 μm, and the grain size is ~10–30 μm, it leads to the estimation that ~10–25% of the whole volume of the fine-grained sample is already liquid at the bulk solidus temperature. The grain size in the as-cast alloys is about ten times larger than in the HPT alloys heated up to 300 °C. Therefore, the magnitude of the observed GB melting heat effect in as-cast alloys is much lower than in HPT samples. However, the starting point of GB melting estimated using the second tangential (Fig. 4) is not very different for as-cast and HPT alloys (Fig. 5). If one carefully compares the DSC melting curves of Al-7034 and Al-2024 alloys in as-received and ECAP-deformed state, one can observe that the melting starts a few K earlier after ECAP (Fig. 2 in Ref. [13] and Fig. 3 in Ref. [14]). The grain size of Al-7034 and Al-2024 samples immediately after ECAP (i.e., before the DSC heating) was ~0.3 μm [13,14].

The GB solidus line appears in the (Al) single-phase region of the Al–Zn phase diagram because the GB wetting

transition by liquid phase proceeds in the (Al)+L two-phase region [48]. The new metastable GB solidus line can be compared with the metastable solvus lines for the formation of GP zones and α phases in the (Al)+Zn two-phase area. The GB solidus line starts at the intersection point between the tie-line of the GB wetting phase transition and the bulk solidus line [49]. It finishes at the bulk melting point of Al. It was possible to observe the melting of GB below the bulk solidus by DSC only because the grain size in the first DSC heating cycle was small enough. Thus, the application of severe plastic deformation in the preparation of such samples is very important. The observed splitting of the solidus line into a conventional bulk solidus and a novel GB solidus can explain the mysterious phenomenon of the high strain-rate superplasticity (HSRS) observed in several nanostructured Al ternary alloys and nanostructured Al metal–matrix composites containing Zn and Mg [3,4,50–58]. The maximum elongation-to-failure increased drastically from 200–300% to 2000–2500% in a very narrow temperature interval of ~10 °C just below the respective solidus temperatures. For a very long time, no satisfactory explanation was offered for this phenomenon.

Owing to the fact that the Al–Zn and Al–Mg systems are the basis of multicomponent alloys which present HSRS, and having observed wetting of GB for these systems, it is suggested that GB pre-melting or pre-wetting is responsible for the HSRS. In that case, a liquid-like thin layer would cover the GB, leading to enhanced plasticity of the materials. Indeed, a GB wetting transition proceeds in binary Al–Zn and Al–Mg systems [48,59]. Considering this hypothesis and using results published on HSRS for Al–Zn–Mg alloys, it could be observed that GB wetting proceeds in multicomponent alloys as well as in binary systems [3,4,54–58]. From the micrographs published in [3,4], the maximum temperature of the GB wetting transition $T_{wmax} = 535$ °C was estimated for the 7xxx Al–Mg–Zn alloys (Fig. 8). Above T_{wmax}, all high-angle GB are completely wetted by the melt. At 475 °C, ~50% of GB are wetted (see $T_{w50\%}$ in Fig. 8). Unfortunately, the micrographs of the Al–Mg–Zn alloys published in Refs. [3] and [4] do not enable one to estimate $T_{wmin} < T_{w50\%}$. The hypothetical GB solidus lines are shown in Fig. 8. They start from the intersection of GB wetting tie-lines T_{wmax} and $T_{w50\%}$ with the bulk solidus and finish at the melting point of Al. The scheme in Fig. 8 demonstrates that, at higher temperatures close to the bulk solidus line, more GBs in the (S) area are liquid-like than at lower temperatures. It can be seen that maximum elongation-to-failure values observed in [3,4,50–58] can be explained by the shape of GB solidus lines and, therefore, by the presence of GB liquid-like layers. At lower Zn and Mg concentrations, the maximum elongation-to-failure values were well below bulk solidus temperature. It corresponds to the high amount of GB completely wetted in the S+L area and, respectively, a high amount of GB having a liquid-like layer in the S area. With increasing Zn and Mg concentration, the maximum of

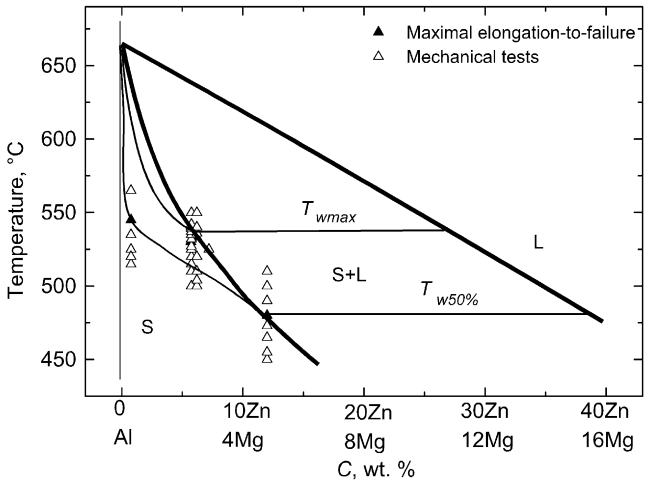

Fig. 8. Pseudobinary phase diagram for 7xxx Al–Zn–Mg alloys (thick lines), containing GB wetting phase transition tie-lines at T_{wmax} and $T_{w50\%}$ (thin lines). Hypothetical GB solidus lines are also shown. Experimental points are taken from Refs. [3,4,54–58]. S marks the one-phase area of solid solution. L marks the one-phase area of liquid. S+L marks the two-phase area where liquid and solid phases are in equilibrium.

elongation-to-failure values first merges with the bulk solidus lines, and then HSRS disappears. This is because the amount of GB completely wetted in the S+L area and of GB with a liquid-like layer in the S area decreases with increasing Zn and Mg concentration. One of the possible mechanisms for superplasticity is GB diffusion. According to the Dorn equation for secondary creep strain rate, it is proportional to the diffusion coefficient controlling the superplasticity process [60]. In [3,4,50–58], the strain-rate increases ~2 to 10 times close to the solidus line. By crossing the GB solidus line, the GB diffusivity increases by one to two orders of magnitude [5,7,8]. The GB mobility, which is also controlled by the mobility of GB atoms, increases ~10 times [43]. Therefore, such an increase can easily explain the onset of HSRS in the fine-grained Al-based alloys [3,4,50–58]. Therefore, it is concluded that GB pre-melting or pre-wetting can be the reason for the HSRS in the nanostructured 7xxx alloys. In [3,4,50–58], the nanocomposites were produced by ball milling and consolidation. However, the nanograined alloys obtained by various SPD methods are most promising from the point of view of their mechanical properties, especial their ability in superplastic forming (for a review, see Ref. [61]).

In Ref. [62], the GB wetting phase transformation was experimentally observed for the first time when GB was wetted not by a liquid, but by a second solid phase. In this work, the microstructure of Zn–10 wt.% Al polycrystals was studied in the temperature range 250–375 °C. The Al-rich phase formed either chains of separated lens-like precipitates or continuous layers at the (Zn)/(Zn) GB upon annealing at different temperatures. The contact angle at the intersection between the (Al)/(Zn) interphase boundaries and the (Zn)/(Zn) GB decreased with increasing temperature. It became zero at a certain temperature, and remained zero above this solid state wetting temperature,

i.e., a continuous (Al) layer covered the (Zn)/(Zn) GB. The fraction of wetted GB increased with increasing temperature and was independent of annealing time. From this work, a very interesting question arises, whether the opposite is true, i.e., can the (Al)/(Al) GB be completely wetted by a layer of Zn? It is a logical hypothesis, as the liquid Al–Zn phase wets (Al)/(Al) GB in solid Al polycrystals [62]. The experiments conducted in this work inevitably witnessed that the Zn particles remain lens-like in all observed (Al)/(Al) GBs between 200 and 270 °C. The contact angles of Zn precipitates in high-angle (Al)/(Al) GB are low, and decrease with increasing temperatures (Fig. 6), but remain non-zero up to the temperature of monotectoid transformation (277 °C [16]). Therefore, full wetting of (Al)/(Al) GB by the Zn solid phase does not occur in the Al–Zn system.

5. Conclusions

1. HPT of as-cast Al–Zn alloys leads to full decomposition of supersaturated (Al) solid solution. The size of both (Al) and Zn grains becomes 10–100 times smaller than in the as-cast state.
2. By the heating of HPT-deformed samples from room temperature to 300 °C, Zn grains dissolve, and equilibrium (Al) solution forms. (Al) remains relatively fine grained. The quick dissolution of Zn is ensured by the very fine-grained structure obtained by HPT, and proceeds close to the equilibrium solvus temperature, i.e., ~100–200 °C higher than the dissolution of metastable GP zones and α phases.
3. The heat of Zn dissolution in (Al) is about two to three times higher than the heat of dissolution for metastable GP zones and α phases in Al–Zn alloys, but it is comparable with the heat of full dissolution for the stable $\eta(MgZn_2)$ phase in Al–Zn–Mg alloys.
4. The satellite endothermic DSC peak is observed below the main melting peak. It is more pronounced in HPT-deformed fine-grained alloys. Melting of the fine-grained (Al) solid solution starts below the bulk solidus line. It can be explained by the presence of layers of liquid-like phase in the (Al) GB between bulk and GB solidus lines. The GB solidus line appears in the (Al) single-phase region of the Al–Zn phase diagram, because the GB wetting transition by liquid phase proceeds in the (Al)+L two-phase region.
5. The formation of liquid-like GB layers close to the solidus temperature explains the phenomenon of high strain-rate superplasticity observed in several nanostructured Al ternary alloys and nanostructured Al metal–matrix composites containing Zn and Mg, in a very narrow temperature interval under the bulk solidus lines. This phenomenon remained unexplained for a long time.
6. Below the monotectoid temperature, i.e., in the (Al)+Zn two-phase area of the bulk phase diagram, the contact angles of Zn precipitates in high-angle (Al)/(Al) GB decrease with increasing temperature, but remain non-zero. Therefore, full wetting of (Al)/(Al) GB by the Zn solid phase does not occur in the Al–Zn system.

Acknowledgements

The investigations were partly supported by INTAS (contract 05-109-4951), the Russian Foundation for Basic Research (contracts 05-02-16528 and 06-03-32875), and the exchange programme between the Russian and Polish Academies of Sciences.

References

[1] Gleiter H. Prog Mater Sci 1989;33:223.
[2] Valiev R. Nat Mater 2004;3:511.
[3] Higashi K, Nieh TG, Mabuchi M, Wadsworth J. Scripta Metall Mater 1995;32:1079.
[4] Takayama Y, Tozawa T, Kato H. Acta Mater 1999;47:1263.
[5] Divinski SV, Lohmann M, Herzig Chr, Straumal B, Baretzky B, Gust W. Phys Rev B 2005;71:104104.
[6] Straumal BB, Mazilkin AA, Kogtenkova OA, Protasova SG, Baretzky B. Philos Mag Lett 2007;87:423.
[7] Straumal B, Rabkin E, Lojkowski W, Gust W, Shvindlerman LS. Acta Mater 1997;45:1931.
[8] Straumal BB, Noskovich OI, Semenov VN, Shvindlerman LS, Gust W, Predel B. Acta Metall Mater 1992;40:795.
[9] Straumal BB, Baretzky B, Mazilkin AA, Phillipp F, Kogtenkova OA, Volkov MN, et al. Acta Mater 2004;52:4469.
[10] Mazilkin AA, Kogtenkova OA, Straumal BB, Valiev RZ, Baretzky B. Def Diff Forum 2005;237:739.
[11] Mazilkin AA, Baretzky B, Enders S, Kogtenkova OA, Straumal BB, Rabkin EI, et al. Def Diff Forum 2006;249:155.
[12] Mazilkin AA, Straumal BB, Rabkin E, Baretzky B, Enders S, Protasova SG, et al. Acta Mater 2006;54:3933.
[13] Gao N, Starink MJ, Furukawa M, Horita Z, Xu Ch, Langdon TG. Mater Sci Forum 2006;503:275.
[14] Starink MJ, Gao N, Furukawa M, Horita Z, Xu Ch, Langdon TG. Rev Adv Mater Sci 2004;7:1.
[15] Valiev R, Islamgaliev R, Alexandrov I. Prog Mater Sci 2000;45:103.
[16] Massalski TB, editor. Binary alloy phase diagrams. Materials Park, OH: ASM International; 1990. p. 238–42.
[17] Dean JA. The analytical chemistry handbook. New York: McGraw Hill; 1995. p. 151 (Standards ASTM D 3417, ASTM D 3418, ASTM E 1356, ISO 11357).
[18] Smith GW. Int J Mod Phys B 1993;7:4187.
[19] Murakami M, Kawano O, Murakami Y. Acta Metall 1969;17:29.
[20] Zahra A, Zahra CY, Mathieu JC. Z Metallkd 1980;71:54.
[21] Jiang XJ, Noble B, Holme B, Waterloo G, Tafto J. Metall Mater Trans A 2000;31:339.
[22] Zahra A, Zahra CY, Laffitte M. Z Metallkd 1979;70:669.
[23] Hirano K, Hori H. J Jap Inst Met 1972;36:97.
[24] Zahra AM, Zahra CY, Jaroma-Weiland G, Neuer G, Lacom W. J Mater Sci 1995;30:426.
[25] Chinh NQ, Lendvai J, Ping DH, Hono K. J Alloys Comp 2004;378:52.
[26] Zahra A, Zahra CY, Lacom W, Degischer HP. J Mater Sci 1982;17:3068.
[27] Honyek G, Kovacs I, Lendvai J, Sinh NH, Ungar T, Loeffler H, et al. J Mater Sci 1981;16:2701.
[28] Zieba P, Williams DB. Microchim Acta 2004;145:107.
[29] Zieba P. Zt Metalkunde 2004;95:230.
[30] Suresh V, Gupta SD. Zt Metalkunde 1986;77:529.
[31] Peterson NL, Rothman SJ. Phys Rev B 1970;1:3264.

[32] Gödény I, Beke DL, Kedves FJ. Phys Stat Solid A 1972;13:K155.
[33] Saada G. Acta Met 1961;9:965.
[34] Beke DL, Gödény I, Kedves FJ. Trans Jpn Inst Met Suppl 1986;27:649.
[35] Aleshin AN, Aristov VYu, Bokstein BS, Shvindlerman LS. Phys Stat Solid A 1978;45:359.
[36] Zieba P, Pawlowski A, Gust W. Def Diff Forum 2001;194:1759.
[37] Friedel J. Dislocations. Oxford: Pergamon Press; 1964.
[38] Blewitt TH, Coltman RR, Redman JK. J Appl Phys 1954;28:651.
[39] Winterberger M. Acta Metall 1959;7:549.
[40] Stølen S, Grønvold F. Thermochim Acta 1999;327:1.
[41] Della Gatta G, Richardson M, Sarge SM, Stølen S. Pure Appl Chem 2006;78:1455.
[42] Sun JQ, Zhang RY, Liu ZP, Lu GH. Energ Convers Manag 2007;48:619.
[43] Molodov DA, Czubayko U, Gottstein G, Shvindlerman LS, Straumal BB, Gust W. Philos Mag Lett 1995;72:361.
[44] Schölhammer J, Baretzky B, Gust W, Mittemeijer E, Straumal B. Interf Sci 2001;9:43.
[45] Straumal B, Sluchanko NE, Gust W. Def Diff Forum 2001;188:185.
[46] Cahn JW. J Chem Phys 1977;66:3667.
[47] Rabkin EI, Shvindlerman LS, Straumal BB. Int J Mod Phys B 1991;5:2989.
[48] Straumal B, López G, Gust W, Mittemeijer E. In: Zehetbauer MJ, Valiev RZ, editors. Nanomaterials by severe plastic deformation fundamentals – processing – applications. Weinheim, Germany: J.Wiley,VCH; 2004. pp. 642–647.
[49] Straumal BB, Zięba P, Gust W. Int J Inorg Mater 2001;3:1113.
[50] Nieh TG, Henshall CA, Wadsworth J. Scripta Metall 1984;18:1405.
[51] Mabuchi M, Higashi K, Okada Y, Tanimura S, Imai T, Kubo K. Scripta Metall 1991;25:2003.
[52] Nieh TG, Gilman PS, Wadsworth J. Scripta Metall 1985;19:1375.
[53] Higashi K, Okada Y, Mukai T, Tanimura S. Scripta Metall 1991;25:2053.
[54] Iwasaki H, Mori T, Mabuchi M, Higashi K. Acta Mater 1998;46:6351.
[55] Baudelet B, Dang MC, Bordeux F. Scripta Metall Mater 1992;26:573.
[56] Imai T, Mabuchi M, Tozawa Y, Murase Y, Kusul J. In: Bhagat RB et al., editors. Metal and ceramic matrix composites: processing modelling & mechanical behaviour. Warrendale, PA: TSM-ASME; 1990. pp. 235–242.
[57] Mabuchi M, Higashi K, Imai T, Kubo K. Scripta Metall 1991;25:1675.
[58] Furushiro N, Hori S, Miyake Y. In: Hori S, et al., editors. Proc. int. conf. superplast., adv. mater., ICSAM-91. Japan Soc. Res. Superplast., Sendai; 1991. pp 557–563.
[59] Straumal BB, López G, Mittemeijer EJ, Gust W, Zhilyaev AP. Def Diff Forum 2003;216–217:307.
[60] Cahn RW, Haasen P, editors. Physical Metallurgy. North-Holland, Amsterdam; 1996. p. 1964.
[61] Valiev RZ, Langdon TG. Prog Mater Sci 2006;51:881.
[62] López GA, Mittemeijer EJ, Straumal BB. Acta Mater 2004;52:4537.